Deviations from Vegard's Law and Evolution of the Electrocatalytic Activity and Stability of Pt-Based Nanoalloys Inside Fuel Cells by in Operando X-ray Spectroscopy and Total Scattering

Journal:	*Nanoscale*
Manuscript ID	NR-ART-02-2019-001069.R1
Article Type:	Paper
Date Submitted by the Author:	27-Feb-2019
Complete List of Authors:	Petkov, Valeri; CMU, Physics Maswadeh, Yazan; CMU, Physics Vargas Tellez, Jorge; CMU, Physics Shan, Shiyao; State University of New York at Binghamton, Department of Chemistry Kareem, Haval; State University of New York at Binghamton, Chemistry Wu, Zhipeng; State University of New York at Binghamton, Chemistry Luo, Jin; State University of New York at Binghamton, Department of Chemistry Zhong, Chuan-jian; State University of New York at, Department of Chemistry Shastri, Sarvjit; Advanced Photon Source, Argonne National Laboratory Kenesei, Peter; Argonne National Laboratory, X-Ray Science Division, Advanced Photon Source

SCHOLARONE™
Manuscripts

ARTICLE

Deviations from Vegard's law and evolution of the electrocatalytic activity and stability of Pt-based nanoalloys inside fuel cells by *in operando* x-ray spectroscopy and total scattering

Valeri Petkov,[a]* Yazan Maswadeh,[a] Jorge Vargas Tellez,[a] Shiyao Shan,[b] Haval Kareem,[b] Zhipeng Wu,[b] Jin Luo,[b] Chuan-Jian Zhong,[b] Sarvjit Shastri [c] and Peter Kenesei [c]

Catalysts for energy related applications, in particular metallic nanoalloys, readily undergo atomic-level changes during electrochemical reactions. The origin, dynamics and implications of the changes for the catalysts' activity inside fuel cells though are not well understood. This is largely because they are studied on model nanoalloy structures under controlled laboratory conditions. Here we use combined synchrotron x-ray spectroscopy and total scattering to study the dynamic behaviour of nanoalloys of Pt with *3d*-transition metals as they function at the cathode of an operating proton exchange membrane fuel cell. Results show that the composition and atomic structure of the nanoalloys change profoundly, from the initial state to the active form and further along the cell operation. The electrocatalytic activity of the nanoalloys also changes. The rate and magnitude of the changes may be rationalized when the limits of traditional relationships used to connect the composition and structure of nanoalloys with their electrocatalytic activity and stability, such as Vegard's law, are recognized. In particular, deviations from the law inherent for Pt-*3d* metal nanoalloys can well explain their behaviour under operating conditions. Moreover, it appears that factors behind the remarkable electrocatalytic activity of Pt-*3d* metal nanoalloys, such as the large surface to unit volume ratio and "size misfit" of the constituent Pt and *3d*-transition metal atoms, also contribute to their instability inside fuel cells. The new insight into the atomic-level evolution of nanoalloy electrocatalysts during their lifetime is likely to inspire new efforts to stabilize transient structure states beneficial to their activity and stability under operating conditions, if not synthesize them directly.

Introduction

Fuel cells are a viable alternative to mankind's reliance on fossil fuels. Fuel cells though are not on the mass market yet, mostly because of the lack of efficient catalysts for the sluggish chemical reactions driving cells' operation, such as the oxygen reduction reaction (ORR). The reaction takes place at the cathode of virtually all fuel cells, where oxygen molecules adsorbed and reduced at the cell's cathode react with protons supplied by the cell's anode to form water. Studies have shown that the ORR proceeds via a number of steps including, among others, a dissociative adsorption of molecular oxygen and removal of reaction intermediates such as atomic oxygen and hydroxyl (OH) groups. The current understanding is that an efficient catalyst for the ORR would bind oxygen molecules with sufficient strength to facilitate the breaking of O=O bonds but infirmly enough to release the reaction intermediates and product

when the reaction ends.[1-4] Pure Pt is the best monometallic catalyst for the ORR but is not suitable for large-scale application largely because it is one of the world's rarest metals. Extensive studies carried out so far found that nanoalloys of Pt with earth-abundant *3d*-transition metals (TMs), such as Ni, Co and Cu, are rather affordable and more active catalysts for the ORR as compared to pure Pt nanoparticles (NPs).[5-8] Qualitatively, the improvement has been attributed to charge transfer from the less electronegative TM atoms to the more electronegative Pt atoms (~1.9 for Ni, Co and Cu *vs.* 2.3 for Pt) and, furthermore, shortening of Pt-Pt bonding distances, *i.e.*, compressive strain. The latter occurs because of the difference in the elemental size of Pt (2.778 Å), Ni (2.49 Å), Co (2.50 Å) and Cu (2.56 Å) atoms. Both the charge transfer and compressive strain are thought to lead to a downshift of the *d*-electron states of surface Pt atoms with respect to the Fermi level of the nanoalloy particles, thus reducing the "poisoning" effect of ORR intermediates.[4,8-10] In addition, it is considered that the presence of two types of transition metal atoms in the nanoalloys creates opportunities for manoeuvring of oxygen species over different surface sites, thereby enabling an extra bi-functional mechanism for accelerating the ORR kinetics.[6,8,11-13] Among others, the so-called Pt-skin, Pt-skeleton, TM core-Pt shell, Pt-octahedral and Pt-frame type alloy NPs have emerged as particularly promising.[6,8,14,15] Note that, following the widely adopted definition,

a. Department of Physics and Science of Advanced Materials Program, Central Michigan University, Mt. Pleasant, Michigan 48859, USA.
E-mail: petko1vg@cmich.edu
b. Department of Chemistry, State University of New York at Binghamton, Binghamton, New York 13902, USA.
c. X-ray Science Division, Advanced Photon Source, Argonne National Laboratory, Argonne, Illinois 60439, USA.
† Footnotes relating to the title and/or authors should appear here.
Electronic Supplementary Information (ESI) available: [details of any supplementary information available should be included here]. See

here we use the term "nanoalloy" to describe any nanosized mixture of Pt and TM metallic species, irrespective of the degree of their mixing and way of mixing.[16]

Unfortunately, the very promising nanoalloy catalysts developed so far cannot quite deliver the expected high performance inside fuel cells. The reason is that under operating conditions, TM species would leach from the catalyst particles, thereby adversely affecting their electrocatalytic activity. Currently, the problem is alleviated by annealing the NPs at high temperature to achieve better alloying between the Pt and TM species, including formation of Pt-TM intermetallics. Conditioning the NPs by chemical etching to remove the "unalloyed" TM species before the catalyst is utilized, controlled electrochemical de-alloying of the NPs to achieve a TM core-Pt shell or Pt-frame type structure and depositing Pt layers on the surface of pre-made TM-rich cores have also been found useful. Typically, these efforts are guided and their success evaluated using separately obtained characteristics of the pristine, purposely conditioned/de-alloyed and used catalyst particles such as their composition, size, atomic arrangement, lattice parameter, and electronic structure of the constituent Pt and TM species. To facilitate the efforts, semi-empirical relationships borrowed from metallurgy, such as the Vegard's law, are used to connect the composition and structure of studied catalysts with their electrochemical activity and stability. [17-34] Here we scrutinize this relationship by studying simultaneously the composition, atomic-level structure and activity of binary and ternary Pt-TM nanoalloy catalysts for the ORR (TM=Ni, Co and/or Cu) as they evolve from a pristine to active state and then function for hours at the cathode of an operating proton exchange membrane fuel cell (PEMFC). The study involves combined energy-dispersive synchrotron x-ray spectroscopy (EDS) and total scattering coupled to atomic pair distribution function (PDF) analysis, including 3D structure modeling.[35]

Experimental

Binary and ternary Pt-TM alloy NPs with a broad range of compositions were synthesized by a wet chemistry route described in the Supplementary Information (SI). The as-synthesized NPs were deposited on carbon black and subjected to a post-synthesis treatment involving heating at 260 °C in N_2 for 30 min followed by heating at 400 °C in 15 vol. % H_2 for 120 min. The treatment helps both clean up the surface of the NPs from organic capping agents and maximize the degree of alloying of the constituent Pt and TM species. The overall chemical composition of post-synthesis treated Pt-TM NPs, hereafter referred to as fresh NPs, was determined by inductively coupled plasma atomic emission spectroscopy (ICP-AES) and confirmed by independent EDS as described in the SI. The fresh NPs comprising Ni and Co species appeared with an overall chemical composition of $Pt_{68}Co_{32}$, $Pt_{58}Ni_{17}Co_{25}$, $Pt_{37}Ni_{39}Co_{24}$ and $Pt_{12}Ni_{53}Co_{35}$. Those comprising Cu species instead of Ni or Co species appeared with a composition of $Pt_{21}Ni_{40}Cu_{39}$ and $Pt_{51}Co_{18}Cu_{31}$. For completeness, standard Pt and $Pt_{79}Ni_{21}$ NPs were also studied.

The size and shape of the fresh NPs were determined by Transmission Electron Microscopy (TEM), as described in the SI. Exemplary TEM and high-resolution (HR)-TEM images are shown in Figure S1. As can be seen in the Figure, the NPs are approximately 8.7 (±1.5) nm in size and rounded in shape. In addition, the NPs possess a good degree of crystallinity as indicated by the clear lattice fringes appearing in the respective HR-TEM images.

A PEMFC optimized for total x-ray scattering studies, involving high-energy x-ray diffraction (HE-XRD) and atomic PDF analysis of the diffraction data, was used to reveal the simultaneous changes in the atomic-level structure and catalytic activity of Pt-TM alloy NPs under operating conditions. The PEMFC is shown in Figure S2. Membrane electrode assemblies (MEAs) for the PEMFC were prepared as described in the SI. Here we concentrate on changes caused by the highly corrosive environment at the PEMFC cathode alone, including interfacial acidity, high humidity, elevated temperature and dynamic load cycling. Hence, and following a protocol recommended by DOE,[36] the PEMFC was cycled between 0.6 V to 1.0 V for about 5 to 6 hours, corresponding to about 1600 potential cycles. During the cycling, humidified hydrogen and nitrogen gas were fed to the PEMFC anode and cathode compartments, respectively, and the operating temperature was maintained at 80 °C. The current output of the PEMFC was non-stop recorded during the potential cycling. Exemplary polarization curves showing the current output of the PEMFC resulting from the repetitive application of external voltages are summarized in Figure 1. In line with the work of others, the curves are seen to collapse with the potential cycling. [37-40] Following the proven practices of *ex situ* catalytic studies, changes in the electrocatalytic activity of the cycled nanoalloys were assessed from changes in the current output of the PEMFC at a fixed potential, in particular 0.9 V on the polarization curves.[1,36,41] As discussed in the SI, the rationale is that this output is sensitive to the formation and reduction of oxygenated surface species, such as Pt(O) and Pt(OH), which are an important factor in determining the kinetics of ORR over the surface Pt-TM nanoalloys. Note that the formation and reduction of Pt(O) and Pt(OH) species is a process actually taking place during the cycling of Pt-TM nanoalloys under humidified atmosphere, be it humidified oxygen, air or nitrogen. [37-45] Furthermore, it has been suggested that a primary route to diminishing the degradation of ORR activity indeed lies through suppressing oxide adsorption up to higher potentials, thus leaving more surface Pt sites available to reduce O_2.[1,36,41] Changes in the area of the polarization curves with the potential cycling, which are related to changes in the oxidation/reduction charge during the cycling, provide an equally informative measure of changes in the ORR activity of the respective nanoalloys (compare data in Figures S3 and S4). Studies have shown, however, that due to intrinsic differences (e.g. in pH, temperature, humidity, cell configuration, MEAs preparation etc.) between laboratory and fuel cell testing of ORR catalyst, full quantitative agreement between measures for electrocatalytic activity derived from data obtained under laboratory and operating conditions cannot be expected. It is important though that trends between different catalysts and with respect to their aging behaviour are correctly represented.[46, 47] Hence, changes in the "redox" current at 0.9 V on the polarization curves with the potential cycling were represented in terms of percentage differences from the initial value of the current and considered merely as a quantity describing relative changes in the apparent (as measured) ORR activity of cycled nanoalloys. Relative changes in ORR activity derived as described above were cross-checked against
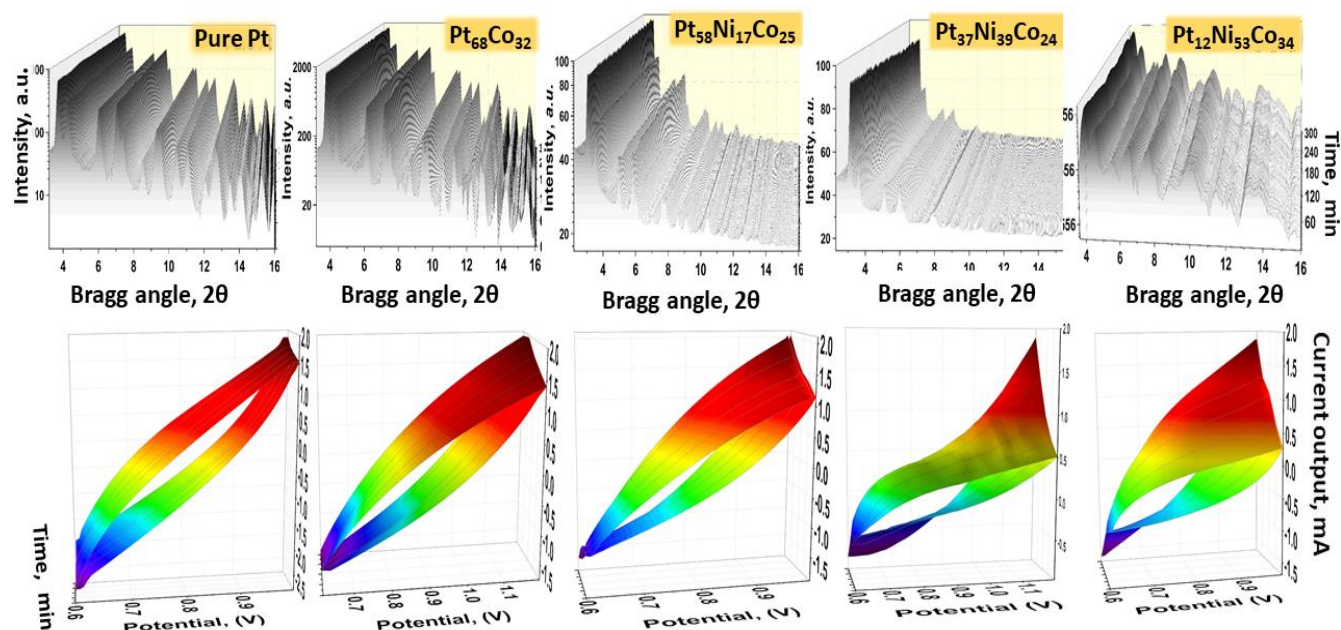
ARTICLE

Fig. 1 (top row) Experimental *in operando* HE-XRD patterns (~300 in number) for pure Pt and Pt-TM alloy NPs (TM=Ni, Co) cycled inside the PEMFC for about 5 hours. (bottom row) Also shown are the concurrently collected polarization curves (~1600 in number) representing the PEMFC current output resulted from the repetitive application of external voltage in the range from 0.6 V to 1.0 V. The curves tend to collapse with the potential cycling indicating a deterioration in the apparent ORR activity of the NPs for reasons discussed in the text. As shown in Fig. S5, the magnitude and rate of the collapse with the potential cycling is significant and different for the different NPs. Selected polarization curves are shown in Figure S3.

similarly normalized data for changes in ORR activity obtained on a standard 3-electrode cell. Results from the comparison are shown in Figure S5. As can be seen in the Figure, overall, trends of data for relative changes in ORR activity of Pt-TM nanoalloys obtained by laboratory and *in operando* experiments agree, testifying to the reliability of the results reported here.

HE-XRD experiments were conducted at the 1-ID-C beamline of the Advanced Photon Source at the Argonne National Laboratory using a focused x-ray beam with energy of 84.917 keV (λ=0.1458 Å).[48] Details of the experimental set-up are shown in Figure S2. HE-XRD patterns were collected in intervals of 1 min throughout the PEMFC operation. Exemplary *in operando* HE-XRD patterns are shown in Figure 1. As can be seen in the Figure, the patterns exhibit a few strong Bragg-like peaks at low diffraction angles and almost no sharp features at high diffraction angles. The average size of the NPs cycled inside the PEMFC was determined from the FWHM of the strongest Bragg-like peak in the respective HE-XRD patterns using the Scherrer formalism.[49] Results showed that the average size of cycled particles increased by about 10 % to 15 % at most. The so-called geometric surface area (GSA) of nanoalloy catalysts is inversely proportional to the size of nanoalloy particles. In turn, generally, the GSA is proportional to the so-called electrochemical active surface area (ECSA) of the catalysts, which is an important factor in determining their mass activity for ORR. [36,41,50] The GSA of the cycled catalyst particles was calculated from the experimental values for their average size and found to diminish gradually during the PEMFC operation. The rather diffuse nature of the *in-operando* HE-XRD patterns though prevented applying well-established procedures for in-depth structural characterization of bulk metals and alloys to the nanoalloy particles studied here. Therefore, the

patterns were analysed in terms of atomic PDFs shown in Figure S6. Details of the derivation of atomic PDFs from HE-XRD patterns can be found in the SI. Here it is to be underlined that experimental total x-ray scattering data, *i.e.*, data comprising both Bragg-like and diffuse x-ray intensities, and so their Fourier counterparts, the atomic PDFs, reflect ensemble-averaged structural features of all metallic alloy NPs sampled by the x-ray beam in a way traditional powder XRD patterns reflect ensemble-averaged structural features of all polycrystalline particles sampled by the x-ray beam in those experiments. Using NP-ensemble averaged structural features to understand and explain NP-ensemble averaged functional properties (e.g. catalytic, magnetic, optical, etc.) puts the exploration of atomic-level structure and functionality of metallic alloy NPs on the same footing.[51]

EDS spectra were taken concurrently with the HE-XRD patterns, that is, in intervals of 1 min. Exemplary EDS spectra are shown in Figure S7. From the spectra, changes in the overall chemical composition of the catalyst particles during the PEMFC operation were determined following standard procedures.[52] The observed changes in the EDS spectra, *i.e.*, chemical composition of the cycled NPs and the concurrent change in their average size signal the presence of an effective mass transport within the cathode side of MEAs. The magnitude of the mass transport was evaluated by measuring and comparing the elemental and mass distribution (loading) of the catalyst particles over the PEMFC cathode at the beginning and end of the cycling. The measurements were done by scanning a 4.5 mm by 4.5 mm cross section of the MEAs using an x-ray beam with a footprint of about 40 μm by 20 μm. Exemplary maps of the elemental and mass distribution of pure Pt and Pt-TM alloy NPs over the scanned MEA's area are shown in Figures 2, 3

and S8. The maps reveal that, during the PEMFC operation, the NPs gather in some and largely disappear from other spots of the MEAs. The particle's chemical composition fluctuates over the MEAs in a
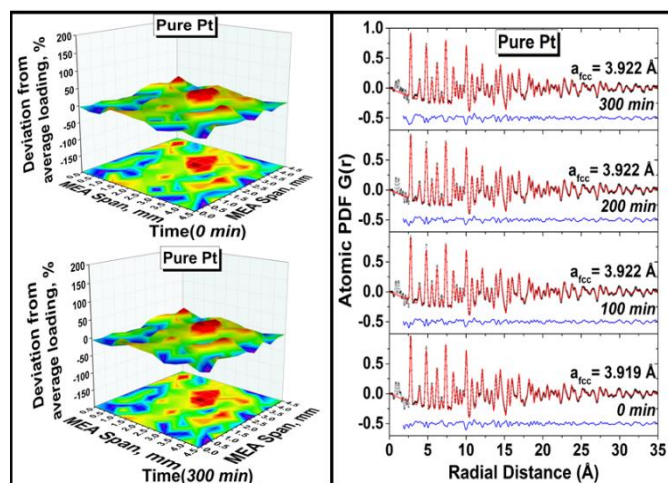

Fig. 2 (left) Mass distribution (loading) of fresh (top row) and 300 min cycled (bottom row) Pt NPs over a 4.5 mm x 4.5 mm area of the MEA. The distribution does not exhibit large fluctuations about the average catalyst loading for that area. **(right)** Experimental (symbols) and computed (red line) atomic PDFs for fresh and cycled Pt NPs. The computed PDFs are derived from a model featuring a uniform fcc-type lattice. The duration of cycling and refined parameter of the model fcc-lattice are given for each data set. Residual difference (blue line) between the experimental and computed PDF data is shifted by a constant factor for clarity. Modeling quality factors, R_w, defined in the SI, for all fits are in the order of 15 ($\pm$ 3) %.

similar manner, though to a much smaller extent.

Experimental atomic PDFs derived from *in operando* HE-XRD patterns collected from different spots of the MEA loaded with $Pt_{12}Ni_{53}Co_{35}$ alloy NPs undergone 1500 potential cycles are shown in Figure S9. The PDFs are similar to each other, indicating that the atomic-level structure of cycled NPs positioned at different spots of the MEAs evolves in a similar manner during the PEMFC operation. Note that the studied nanoalloys were not conditioned prior the *in operando* experiments because it would had prevented an accurate assessment of the effect of the harsh operating conditions inside the PEMFC on their atomic-level structure and, hence, electrocatalytic activity for the ORR. Thus, the collection of experimental data, including the PEMFC current output, HE-XRD patterns and EDS spectra, started as soon as the MEAs loaded with fresh NPs were placed inside the PEMFC and external voltage was applied.

Results and discussion

A Traditional Analysis of the Experimental Difraction Data

To ascertain the structure type of fresh and cycled pure Pt and Pt-TM alloy NPs, the respective experimental atomic PDFs were approached with a simplistic model constrained to an fcc-type crystal structure. The model made sense because the crystalline counterparts are fcc metals and alloys. [53] The unit cell parameter of the lattices was refined such that model-derived atomic PDFs approached the corresponding experimental PDFs as closely as

possible. Computations were done with the help of the program PDFgui. [54]

As can be seen in Figure 2(right), atomic PDFs for fresh and cycled pure Pt NPs are very well approximated with a model featuring a uniform fcc-type structure (*S.G.* Fm-3m). In line with the results of others, [55-57] the lattice parameter for fresh Pt NPs (3.919 Å) appears slightly shorter than the bulk value of 3.924 Å. It approaches the bulk value when the NPs are cycled for 5 hours. As can be seen in Figure 3(right), the atomic PDF for fresh $Pt_{68}Co_{32}$ alloy NPs is very well approximated with a model featuring a chemically ordered (Pt_3TM) fcc-type structure (*S.G.* Pm-3m) with a lattice parameter of 3.855 Å. The parameter is shorter than that for fresh Pt NPs, which is to be expected considering the difference in the elemental size of Co and Pt atoms. A model featuring a chemically disordered fcc-type structure (*S.G.* Fm-3m) with a lattice parameter of 3.862 Å approximates very well the PDF for cycled $Pt_{68}Co_{32}$ alloy NPs. As can be seen in Figure 4(a), the atomic PDFs for fresh and cycled $Pt_{58}Ni_{17}Co_{25}$ alloy NPs are reasonably well approximated with a model featuring a chemically disordered fcc-type structure (*S.G.* Fm-3m). The lattice parameter for fresh $Pt_{58}Ni_{17}Co_2$ alloy NPs (3.825 Å) is shorter than that for fresh $Pt_{68}Co_{32}$ alloy NPs, reflecting the larger percentage of TM species in the former as compared to that in the latter. The fcc-lattice parameter for $Pt_{58}Ni_{17}Co_{25}$ alloy NPs undergone 5 hours of electrochemical cycling increases to 3.838 Å. Data in Figure 4(b) indicate that fresh $Pt_{37}Ni_{39}Co_{24}$ alloy NPs are disordered Pt-TM nanoalloys with an fcc-lattice parameter of 3.750 Å. Major features in the PDFs for cycled $Pt_{37}Ni_{39}Co_{24}$ alloy NPs are reasonably well reproduced by a model based on a 3D periodic fcc-type structure. However, the agreement between the model-derived and experimental PDF data is seen to deteriorate with the potential cycling (see the increasing residual difference between the experimental and model PDF data shown as a blue line below the respective fits). The observation indicates that, under operating conditions, the arrangement of Pt and TM species in the cycled $Pt_{37}Ni_{39}Co_{24}$ alloy NPs becomes increasingly dissimilar to that in a uniform fcc-type structure. Nevertheless, $Pt_{37}Ni_{39}Co_{24}$ alloy NPs cycled for 5 hours still may be assigned a relevant fcc-lattice parameter of 3.789 Å. A model envisioning a uniform fcc-type lattice barely reproduces the experimental PDF data for both fresh and cycled $Pt_{12}Ni_{53}Co_{35}$ nanoalloy particles (see Figure 4c). Using fit results and position of individual peaks in the experimental PDF data, fresh and 5 hours cycled $Pt_{12}Ni_{53}Co_{35}$ NPs were assigned an apparent fcc-lattice parameter of 3.639 Å and 3.740 Å, respectively. Results from the traditional analysis of the experimental PDF data for fresh and 300 min cycled pure Pt and Pt-TM alloy NPs are summarized in Table S1. Data in Figures 3, 4 and Table S1 show that the lattice parameter for Pt-TM alloy NPs increases with the potential cycling, reflecting the significant loss of TM atoms and related to it relaxation of the compressive stresses experienced by Pt atoms remaining in the cycled particles. The mutual distribution of Pt and TM atoms in the nanoalloys though is well captured only for the NPs rich in Pt species. That is because models constrained to an fcc-type lattice pertain to 3D periodic Pt-TM structures wherein distinct atoms can form only a few possible chemical patterns (e.g. an ordered or disordered fcc alloy) whereas the arrangement of distinct atoms observed with the typically non-3D periodic metallic alloy NPs can be rather diverse. To reveal how Pt

and TM species in Pt-TM alloy NPs are intermixed together, we conducted nanophase analysis of the NPs, as described below.

B Nanophase Analysis Substantiated by Experimental EDS, TEM and PDF Data

carried out with LAMMPS, using a second nearest-neighbour modified embedded atom method potentials for Pt and TM metals.[60,61] The relaxed nanostructures were tested and, when found plausible, refined against the experimental PDF data by reverse Monte Carlo computations. More details can be found in the SI. A model nanostructure relaxed in terms of energy by MD
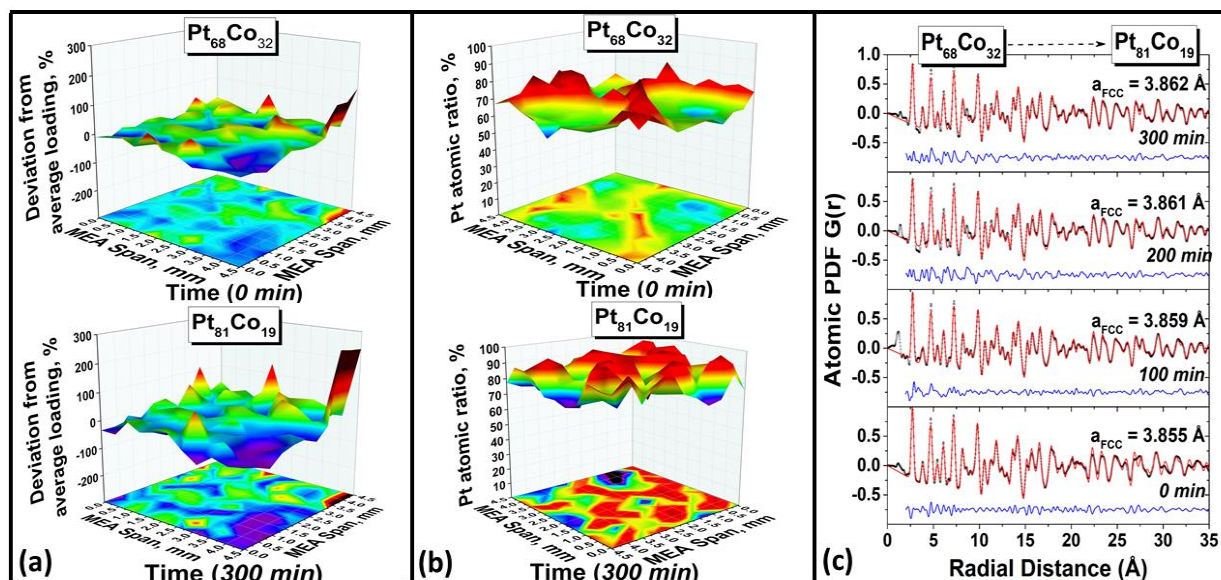

Fig. 3 (a) Mass distribution (loading) of fresh (top row) and 300 min cycled (bottom row) $Pt_{68}Co_{32}$ alloy NPs particles over a 4.5 mm x 4.5 mm area of the MEA. The distribution is irregular showing large fluctuations (up to ~ 100 %) from the average catalyst loading for that area. (b) Distribution of Pt species over the same MEA area for fresh (top row) and cycled (bottom row) NPs. The distribution is normalized against the average chemical composition of the NPs, as determined by EDS. Note that, due to leaching of Co species during the PEMFC operation, the average chemical compositions of the NPs changes from $Pt_{68}Co_{32}$ to $Pt_{81}Co_{19}$. Nevertheless, the fluctuations of the chemical composition of the NPs at different spots of the MEA do not exceed a few at. %. (c) Experimental (symbols) and computed (red line) atomic PDFs for fresh and cycled $Pt_{68}Co_{32}$ alloy NPs. The computed PDFs are derived from a structure model featuring a uniform fcc lattice. The duration of cycling and refined parameter of the model fcc-lattice are given for each data set. Residual difference (blue line) between the experimental and computed PDF data is shifted by a constant factor for clarity. Modeling quality factors R_w, defined in the SI, for all fits are in the order of 18 ($\pm$ 3) %.

It has been recognized that the large surface to unit volume ratio affects strongly the thermodynamic properties of metallic NPs and so can lead to a stabilization of particular atomic and chemical ordering patterns in the NPs at the expense of others. The patterns can endow the NPs with novel functional properties such as, for example, improved electrocatalytic activity for the ORR. Furthermore, it has been recognized that under the constraint of a small particle size, the patterns may not necessarily have bulk counterparts.[58,59] Hence, to determine the atomic ordering in fresh Pt-TM alloy NPs and how it evolves with the potential cycling in better detail, we generated several plausible nanostructures for the respective NPs. The nanostructures included near phase segregated "sandwich"-, Janus-, TM core-Pt shell and Pt core-TM shell type NPs. Structures representing NPs with a Pt-enriched core and TM-enriched near surface region, and vice versa, were also generated. To be as realistic as possible, the nanostructures reflected the size (~11000 atoms), shape (rounded) and chemical composition of the modeled NPs as obtained by the *ex situ* TEM, HR-TEM, ICP-AES, *in operando* EDS and HE-XRD experiments conducted here. For completeness, pure Pt NPs were also modeled. The models were relaxed in terms of energy, *i.e.*, stabilized at atomic scale, by Molecular Dynamics (MD) computations. The computations were

and minimizing the residual between the model computed and experimental PDF data was considered a realistic representation of the nanophase content/chemical pattern of the modeled NPs. Here it is to be underlined that determining the (nano)phase type of materials through comparing experimental diffraction data with data for reference phases, known as "phase-analysis", is a widely applied technique in materials research and technology.[62] The success of nanophase analysis of ORR metallic alloy nanocatalyst using MD and *in operando* PDF data has already been demonstrated in our prior studies.[63] Extra evidence is provided in Figure S10. As an example, results from the nanophase analysis of $Pt_{12}Ni_{53}Co_{35}$ nanoalloy particles undergone potential cycling inside the PEMFC are shown in Figure 5. The results indicate that, among others tested (see Figure 5a), a model envisioning NPs with a core entirely formed of TM atoms and surface exhibiting isolated islands of Pt atoms (see Fig. 5b) performs best. When cycled for 100 min, the NPs become of a fully TM core-Pt shell type. Upon further potential cycling, the NPs suffer extra loss in TM species and become of a rich TM core-rich Pt shell type. The respective nanostructure models are shown in Figure S11 in better detail. Results from the nanophase analysis of pure Pt and Pt-TM alloy NPs

studied under PEMFC operating conditions are summarized in Figure 6.

B Composition, Structure, Stability and Electrocatalytic Activity of

strain and restructuring of the nanoalloys.[23,28,64] Results of the studies conducted here help reveal the individual contributions of these factors to ORR activity losses occurring under operating conditions in more detail. In particular, fresh $Pt_{68}Co_{32}$ alloy NPs
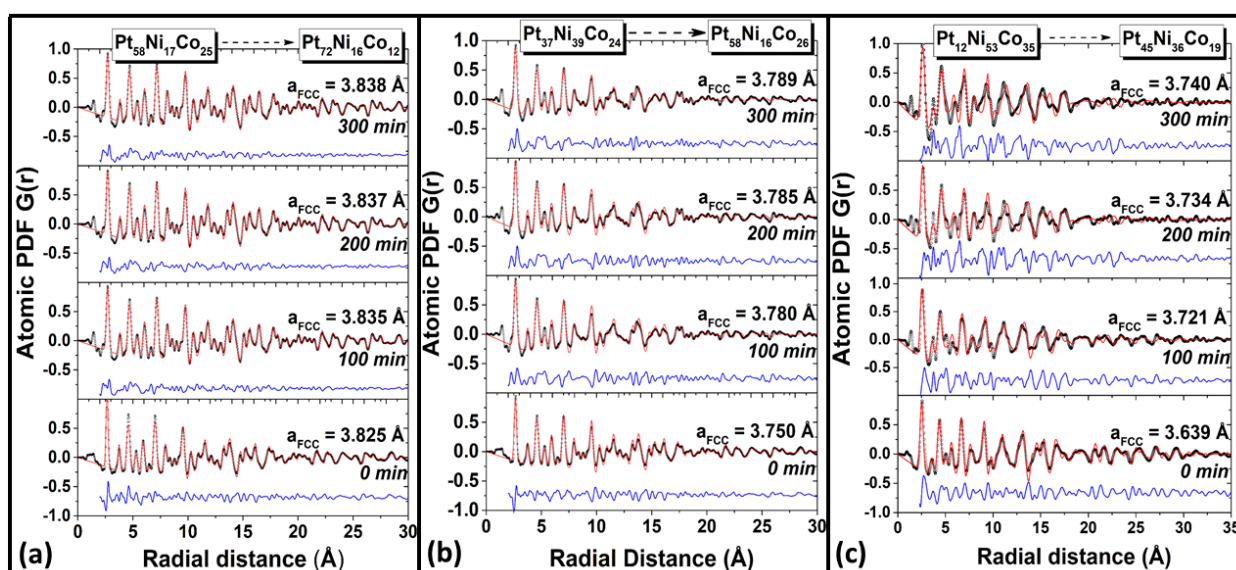

Fig. 4 Experimental (symbols) and computed (red line) atomic PDFs for fresh and cycled **(a)** $Pt_{58}Ni_{17}Co_{25}$, **(b)** $Pt_{37}Ni_{39}Co_{24}$ and **(c)** $Pt_{12}Ni_{53}Co_{35}$ alloy NPs. The computed PDFs are derived from a model featuring a uniform fcc-type lattice. The duration of cycling and refined parameter of the model fcc-lattice are given for each data set. Residual difference (blue line) between the experimental and computed PDF data is shifted by a constant factor for clarity. Modeling quality factors R_w, for fresh and cycled $Pt_{58}Ni_{17}Co_{25}$ are in the order of 19 ($\pm$ 3) %. The modeling quality factor for fresh $Pt_{37}Ni_{39}Co_{24}$ NPs is 20 %. The modeling quality factor for 300 min cycled $Pt_{37}Ni_{39}Co_{24}$ NPs deteriorates to 27 %. Modeling quality factors for both fresh and cycled $Pt_{12}Ni_{53}Co_{35}$ NPs are in the order of 30 % to 40 %, indicating that Pt and TM species in the NPs do not sit on the vertices of a uniform fcc-type lattice. Finite size models exhibiting non-uniform patterns describe the NPs to a much better extent (see Figure 5b). Note that, due to leaching of TM species, the relative percentage of Pt in the cycled NPs increases during the PEMFC operation (follow the dotted arrows on top of the plots).

Pt-TM Nanoalloys under Operating Conditions

In operando data indicative of the evolution of the chemical composition, atomic-level strain and apparent electrocatalytic activity of pure Pt and Pt-TM alloy NPs as deposited as deposited on MEAs and cycled inside an PEMFC are summarized in Figure 6. Also shown in the Figure are MD-modeled and PDF-data verified structures representing the (nano)phase state of the NPs. As can be seen in Figure 6a, the intrinsically low atomic-level strain in pure Pt NPs relaxes by a fraction of a percent at the beginning of the potential cycling. Concurrently, the relative, i.e. with respect to the initial state, catalytic activity of the NPs drops by a few percent. The activity gradually diminishes with further potential cycling, most likely due to the gradual decrease of the GSA, and so ECSA, of the NPs.[36,41] Relative losses in ORR activity experienced by fresh Pt-TM alloy NPs at the beginning of the potential cycling are much larger in comparison to pure Pt NPs. Furthermore, the losses appear proportional to the percentage of TM species leached from the NPs and related fast decrease of the atomic-level strain. Such sharp drops in the apparent activity of barely utilized Pt-TM nanoalloy catalysts for ORR, *e.g.* near 50 % drop in the ORR current for fresh $Pt_{35}Ni_{65}$ nanoalloy electrochemically cycled for only a few minutes, have been reported in *ex situ* studies of others (see Figures 9 and 10 in Ref. [28]). The drops have been tentatively attributed to the combined effect of loss in TM species, diminished atomic-level

appear as a chemically ordered nanoalloy. As soon as the PEMFC starts operating, the NPs suffer about 25 % loss in TM species. Concurrently, the compressive strain in the NPs diminishes from 1.9 % to 1.75 % and their apparent ORR activity drops by about 23 %. Ultimately, the particles transform into a chemically disordered nanoalloy whose surface is depleted of Co species. That would be their catalytically active (or "conditioned") state. During further potential cycling (up to 5 hours), the activated NPs lose a small amount of TM(Co) species and relax at atomic level by further 0.05 %. The GSA of the NPs though diminishes by about 10 % and their apparent ORR activity decays further by 15 % (follow the horizontal dotted red line in Figure 6b). Fresh $Pt_{58}Ni_{17}Co_{25}$ particles appear as a near random nanoalloy. When deposited on a MEA and cycled inside a PEMFC, the particles experience near instant 40 % loss in TM species and 30 % loss in ORR activity. Concurrently, the compressive strain in the particles diminishes from 2.65 % to 2.4 %. As a result, they emerge as largely Pt NPs comprising small domains of TM atom, which will be their catalytically active state. During further potential cycling, the NPs relax at atomic level by further 0.05 %, lose a small amount of TM species and have their GSA diminished by about 10 %. As a result, the apparent ORR activity of the NPs decays further by 10 % (follow the horizontal dotted red line in Figure 6c). Within the first 30 min of the PEMFC operation, near random alloy $Pt_{37}Ni_{39}Co_{24}$ alloy NPs suffer about 55 % loss in TM species and transform into nanoalloy particles with a TM-rich

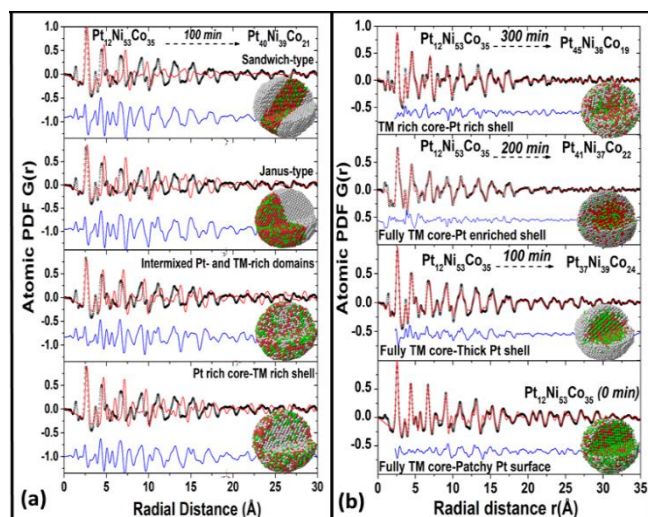**Fig. 5** (**a**) *In operando* (symbols) and computed (red line) atomic PDFs for $Pt_{12}Ni_{53}Co_{35}$ alloy NPs cycled for 100 min. The computed PDFs are derived from structure models shown as insets. Residual difference (blue line) between the experimental and model computed PDFs is shifted by a constant factor for clarity. The difference is large, indicating the inability of the models to reproduce the experimental data. (**b**) *In operando* (symbols) and computed (red line) atomic PDFs for $Pt_{12}Ni_{53}Co_{35}$ alloy NPs cycled for 0, 100, 200 and 300 min. The computed PDFs are derived from structure models shown as insets. Residual difference (blue line) between the experimental and computed PDF data is small, indicating the high quality of the respective models. A more detailed rendition of models in (a) and (b) is given in Figure S11. Pt, Co and Ni atoms are in gray, green and red, respectively. Note that, due to leaching of TM species during the potential cycling, the chemical composition of cycled NPs changes as shown in the plots (follow the horizontal broken lines).

core and Pt-rich shell. Concurrently, the compressive strain in the NPs diminishes from 4.6 % to 4.1 % and their apparent ORR activity drops by about 30 %. When cycled for four extra hours, the NPs keep losing TM species at a slow pace and relax at atomic level by further 0.1 %. In addition, the NPs have their GSA diminished by about 10 %. Concurrently, their apparent ORR activity drops by further 20 % (follow the horizontal dotted red line in Figure 6d). The NPs though preserve their TM rich core-Pt rich shell type structure attained upon activation. The structural evolution of fully TM core-patchy Pt skin type $Pt_{12}Ni_{53}Co_{35}$ particles appears more complex. Initially, the particles experience sharp 65 % loss in TM species and "decompress" by about 2.5 %. As a result, their apparent ORR activity drops by about 30 %. In the process, the NPs acquire a fully TM core-thick Pt shell type structure and their ability to catalyse ORR seems to rebound a bit. The transient fully TM core-thick Pt shell structural state though lasts for about 1 hour of potential cycling. Further cycling induces additional loss in TM species and renders the compressive strain in the NPs undulate about an average value of 5 %. Concurrently, the NPs increasingly become of a TM rich core-Pt rich shell type. Due to structural instability and increased GSA, the apparent ORR activity of the NPs decays further by 30 % (see the dotted red line in Figure 6e). Changes in the apparent ORR activity, composition and atomic-level strain

experienced by the cycled Pt-TM nanoalloy particles from the moment the PEMFC starts operating are summarized in Figure 7b as a function of the percentage of TM species in the respective fresh particles. The residual percentage of TM species and compressive strain in the merely activated, *i.e.*, cycled for up to 30 min only, Pt-TM alloy NPs are summarized in Figure 7a. The enhancement of the actual ORR (MA) activity of the activated Pt-TM NPs in comparison to pure Pt NPs, as obtained from complementary *ex situ* experiments in a standard 3-electrode cell,[13,65-67] is also shown in the Figure. In line with the findings of prior studies on the electrocatalytic activity of partially de-alloyed Pt-TM nanoalloy catalysts for the ORR (TM=Co, Ni and/or Cu),[17,31,64] data sets in Figures 7a and 7b appear strongly correlated to each other. In particular, data in the Figure indicate that relative losses in TM species and ORR activity experienced by the fresh Pt-TM nanoalloy catalysts upon "activation" inside the PEMFC are commensurate with the initial content of TM species in the NPs. The same pertains to the concurrent near sudden drop in the atomic-level stresses. Furthermore, the electrocatalytic activity of merely activated Pt-TM nanoalloys appears commensurate with the percentage of TM species retained in the NPs and related to it residual compressive strain, which, in turn, are commensurate with their values for the fresh nanoalloys.

According to Pauling's theory of chemical bonding and independent experiments, changes in (bonding) distances between nearby atoms and the spatial/energy distribution of the valence *d*-electrons of the atoms involved are intimately coupled and so may not be considered apart.[68-71] Data for the systematic changes in the local atomic strain (see Figure 7a, b) and shifts in the core-level binding energies for fresh Pt-TM nanoalloys (see Figure S13) well illustrate this interrelationship. As TM and Pt atoms in Pt-TM nanoalloys have different Fermi levels, E_f, (e.g. E_f ~9.7 eV for Ni, 10.5 eV for Co, 9.0 for Cu *vs.* 8.8 eV for Pt), charge may be expected to flow from the former towards the latter until the Fermi level in the nanoalloy particles equilibrates. Thus, as is the case with the residual strain, the electronic structure of activated nanoalloys, in particular the *d*-DOS at the Fermi level, would depend on the percentage of TM species retained in the nanoalloys, thereby becoming another composition-dependent factor behind their electrocatalytic activity. Notably, as surface Pt-Pt partial PDFs and distances shown in Figures 8(a-c) indicate, the surface structural characteristics of Pt-TM nanoalloys, fresh or activated, do not match exactly the volume-averaged values, and it is the nanoalloy's surface whereat chemical reactions take place. Typically, the difference is due to surface relaxation effects, including differences in the coordination of atoms inside and at the surface region of the nanoalloys. Altogether, it may be considered that the electrocatalytic activity of Pt-TM NPs deposited on MEAs and briefly exposed to the corrosive environment inside operating PEMFCs is determined by the combined effect of the residual compressive strain, charge transfer due to equilibration of the Fermi level of the constituent TM and Pt atoms, surface relaxation effects and particular nanophase state, including the relative percentage of surface Pt sites available to reduce O_2.

For all activated and further cycled Pt-TM alloy NPs, considerable mass transport is observed all over the cathode side of the respective MEAs (see Figures 2, 3 and S8). The transport is

indicative of exchange of dissolved atomic species between individual Pt-TM NPs, eventually leading to Ostwald ripening, and/or displacement and partial coalescing of nearby Pt-TM NPs. Both processes are known to be gradual and effectively reduce the electrocatalytic activity of functioning Pt-TM nanoalloys through reducing their ECSA.[72] As the time evolution of the experimental GSA data in Figure 6 indicate, losses in ORR activity experienced by "activated & functioning"

Pt-TM nanoalloy catalysts largely arise from mass transport related effects.

C Relationship between the atomic level structure, stability and electrocatalytic activity of Pt-TM Alloy NPs

The likelihood that a nanosized mixture of Pt and TM species would adopt a stable nanoalloy structure and so deliver consistent electrochemical performance can be evaluated through the fundamental thermodynamic relation

$$\Delta G = \Delta H - T\Delta S, \tag{1}$$

where ΔG, ΔH and ΔS is, respectively, the excess free energy, enthalpy and entropy of the nanoalloy, and T is the temperature. The physical meaning of the excess free energy is very simple. If $\Delta G < 0$ alloying between Pt and TM species is energetically favourable, otherwise (nano)phase segregation is more likely to occur. Several factors would affect the structure type and stability of Pt-TM alloy NPs. Among others, the factors include the electronegativity, "size" or volume of the Wigner-Seitz (WS) cell, surface and cohesive energy, Fermi level and valence d-band of the constituent Pt and TM atoms. Finite size effects, including relaxation of surface atoms, shape and faceting of the nanoalloy particles are to be added to the list. [69-70, 73-77] Notably, as discussed above, these factors are also of prime importance to the catalytic activity of Pt-TM nanoalloys. With regard to their atomic-level stability, the different Fermi level of the constituent Pt and TM species and related charge redistribution would make a negative contribution to ΔH, *i.e.* facilitate the formation of Pt-TM nanoalloys. Equilibration of the different WS cells of Pt and TM atoms ($\sim$10.9 Å^3 for Ni, 11.18(fcc)/11.07(hcp) Å^3
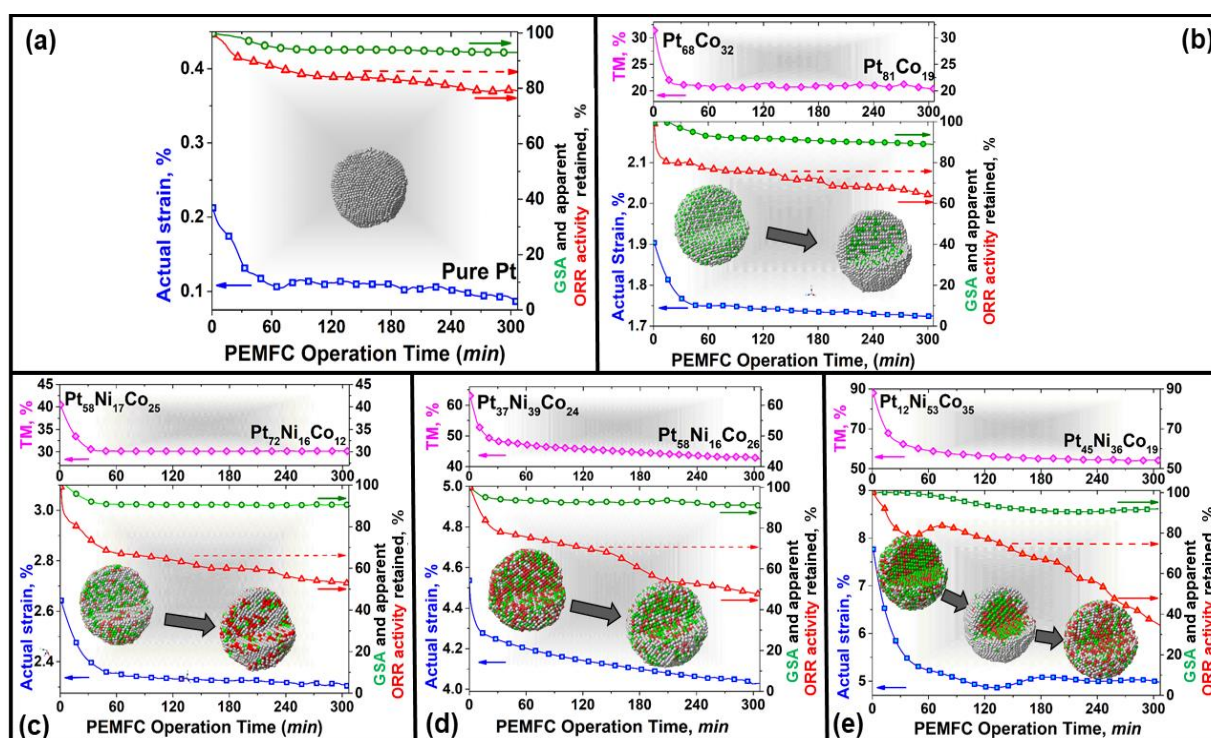

Fig. 6 Evolution of the atomic-level strain (blue symbols & line), GSA (green symbols & line), chemical composition (magenta symbols) and apparent ORR activity for pure Pt and Pt-TM nanoalloy catalysts deposited on the cathode of an operating PEMFC. Changes in the atomic-level strain are obtained from changes in the lattice parameter of the respective NPs as normalized against the lattice parameter of pure Pt. Changes in GSA values are obtained from changes in the FWHM of Bragg-like peaks in the respective *in operando* HE-XRD patterns as normalized against the GSA of fresh catalysts particles. Changes in the apparent electrocatalytic activity are derived from changes in the PEMFC "redox" current at 0.9 V on the respective polarization curves. MD-built & RMC refined 3D models given as insets show the structural state of the fresh (model on the left) and active (model on the right) catalysts. The catalysts undergo the following evolution during the PEMFC operation: **(a)** Fresh Pt NPs relax a bit and retain their fcc-type structure; **(b)** {chemically ordered} $Pt_{68}Co_{32}$ NPs transform into {chemically disordered} NPs whose surface is depleted of Co atoms; **(c)** {near random alloy} $Pt_{58}Ni_{17}Co_{25}$ NPs transform into {largely Pt NPs comprising small domains of TM atoms }; **(d)** {near random alloy} $Pt_{37}Ni_{39}Co_{24}$ NPs transform into {TM rich core-Pt rich shell} NPs; and **(e)** {fully TM core-patchy Pt skin} $Pt_{12}Ni_{53}Co_{35}$ NPs transform into an intermediate active state with a {fully TM core-thick Pt shell type} structure. This state evolves with further cycling and becomes of a {TM rich core-Pt rich shell} type. This is to be expected given both the specific structure of the fresh NPs and extensive change in their chemical composition with cycling. Note that the observed changes in the chemical composition, local strain, overall atomic arrangement and apparent ORR activity are highly correlated in terms of onset, duration and magnitude, indicating the presence of an instant link between these fundamental characteristics of nanoalloy catalysts. A more detailed rendition of the structure models is given in Figure S12. Pt, Co and Ni atoms are in grey, green and red, respectively.

for Co and 11.8 Å^3 for Cu *vs*. 15.1 Å^3 for Pt) to the same atomic volume in the nanoalloy would induce atomic-level stresses and so make a positive contribution to ΔH, *i.e.*, hinder the formation of Pt-TM nanoalloys. The much higher cohesive energy of Pt in comparison to Ni, Co and Cu (~4.44 eV/atom for Ni, 4.39 eV/atom for Co and 3.49 eV/atom for Cu vs 5.84 eV/atom for Pt) would favor clustering in the nanoalloys, including the formation of a TM core-Pt shell type structure. [4,70,74, 77] Furthermore, generally, the smaller TM and large size Pt atoms would tend to segregate towards the nanoalloy's interior and surface, respectively, for minimizing atomic level stresses.

This seems to be the case with fresh $Pt_{12}Ni_{53}Co_{35}$ alloy NPs, which appear with a fully TM core and patchy Pt surface. Attaining a chemically ordered structure at a particular concentration of the intermixed Pt and TM species, *i.e.*, forming an Pt-TM intermetallics,

could also reduce the strain energy and so make a negative contribution to ΔH. This seems to be the case with fresh $Pt_{68}Co_{32}$ alloy NPs. At the same time, due to the loss of complete randomness, the configurational entropy ΔS would increase, making a positive contribution to ΔG. Adding a third component to a binary Pt-TM nanoalloy would increase that entropy and lead to the formation of a chemically disordered ternary nanoalloy, which seems to be the case with fresh $Pt_{58}Ni_{17}Co_{25}$ and $Pt_{37}Ni_{39}Co_{24}$ alloy NPs. Certainly, the structure type and stability of Pt-TM nanoalloys would depend not only on the balance of the above listed factors but also on details of the nanoalloys' synthesis, post-synthesis treatment and working environment (*e.g.* liquid electrolite in 3-electrode cells vs humidified gas-phase evirionment in PEMFCs). Thus, the relationship between
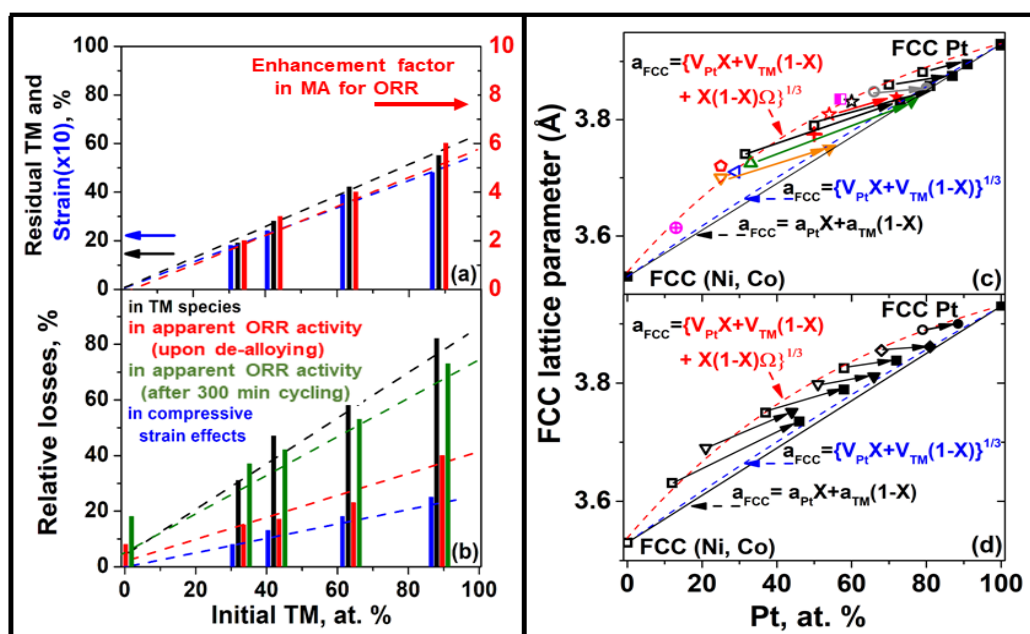

Fig. 7 (a) Residual TM percentage (black bars) and atomic-level strain (blue bars) in partially de-alloyed Pt-TM NPs. Enhancement (red bars) in the electrocatalytic activity (MA for ORR) of de-alloyed/activated NPs in comparison to pure Pt NPs obtained by complementary *ex situ* experiments. Dotted lines emphasize the correlation between the composition, structure and catalytic activity of the NPs. **(b)** Relative losses in TM species (black bars) and apparent activity (initial loss/red bars and total loss/green bars) experienced by fresh Pt-TM alloy NPs inside the operating PEMFC. Changes in the local atomic strain (blue bars) are also shown. Comparison between the respective data sets in *(a)* and *(b)* indicate that, regardless having suffered large loss in activity in comparison to their pristine state, partially de-alloyed Pt-TM NPs perform better as ORR catalysts in comparison to pure Pt NPs. **(c)** Literature data for the fcc-lattice parameters of purposefully de-alloyed (closed symbols) and respective fresh (open symbols) Pt-TM alloy NPs (TM=Ni, Co and/or Cu). Data in black are for 4 nm Pt-Ni particles synthesized at 160 °C to 240 °C.[17] Data in gray are for commercial (E-Tek) 5.4 nm Pt-Co particles.[18] Data in green are for 20 nm polyhedral Pt-Ni particles.[19] Data in orange are for 5 nm Pt-Cu particles annealed at 950 °C.[6] Magenta rectangle denotes data for 3 nm wide and 100 nm long $Pt_{59}Ni_{49}$ NWs annealed at 260 °C.[92] Red star denotes data for sub-nanometer PtNiCo nanowires synthesized at 160 °C.[20] Red cross denotes data for space-confined 3 nm Pt-Ni particles annealed at 850 °C.[21] Red pentagon denotes data for 3 nm Pt-Co particles annealed at 950 °C.[22] Crossed magenta circle denotes data for 12 nm Pt-Ni particles annealed at 400 °C.[23] Crossed blue square denotes data for sputtered Pt-Ni nanoalloys.[28] Red stars denotes data for 9 nm Pt-Ni octahedra synthesized at 230 °C.[24] **(d)** FCC-lattice parameters for 300 min cycled (closed symbols) and respective fresh (open symbols) Pt-TM alloy NPs obtained by *in operando* experiments. Circles denote $Pt_{79}Ni_{21}$ NPs discussed in ref. [87]. Rhombuses denote data for $Pt_{68}Co_{32}$ NPs. Squares denote data for $Pt_{58}Ni_{17}Co_{25}$, $Pt_{37}Ni_{39}Co_{24}$ and $Pt_{12}Ni_{53}Co_{35}$ NPs. Triangles denote data for $Pt_{51}Co_{18}Cu_{31}$ and $Pt_{21}Ni_{40}Cu_{39}$ NPs. In **(c)** and **(d)** blue dotted lines represent the expected composition dependence of the lattice parameter for Pt-TM random alloys obtained from the elemental volumes of Pt and TM species (*Eq. 3*). Red dotted lines represent the expected composition dependence of the lattice parameter for Pt-TM alloy obtained from the elemental volumes of the intermixed atomic species plus a quadratic correction term involving a quantity Ω referred to as an "excess volume" in the text (*Eq.* 4). Slanted black lines represent the composition dependence of the lattice parameter for Pt-TM random alloys as predicted by Vegard's law *(Eq. 2)*. Solid arrows link data for a given pair of cycled and respective fresh catalysts.
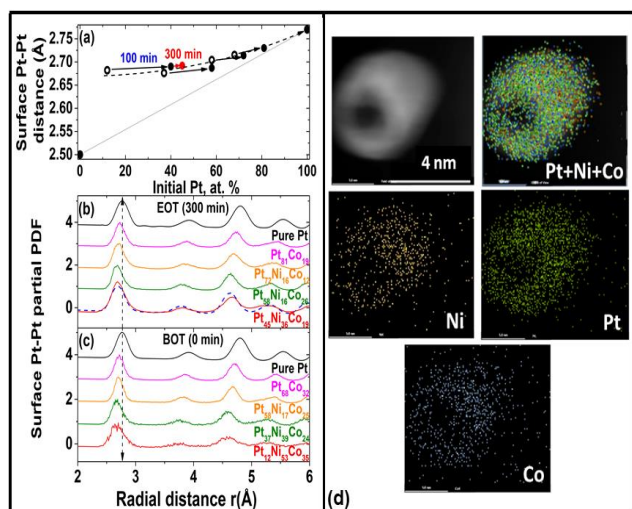
ARTICLE

Journal Name

Fig. 8 (a) Average surface Pt-Pt distance in fresh (open circle) and 300 min cycled (solid circle) pure Pt and Pt-TM alloy NPs. The distance is obtained from the position of the first peak in the surface Pt-Pt partial PDFs for fresh (beginning of test/BOT) and 300 min cycled (end of test/EOT) NPs computed from the respective 3D models shown in Figure 6. The PDFs are shown in **(c)** and **(b),** respectively. Broken line in **(a)** is a guide to the eye. Solid slanted line in **(a)** connects the bulk values for TM-TM and Pt-Pt bonding distances. Vertical broken lines in **(b)** and **(c)** mark bulk Pt-Pt bonding distance. **(d)** Representative HAADF-STEM image and elemental maps of a $Pt_{45}Ni_{33}Co_{22}$ nanoparticle cycled for 600 min.[87] Due to the prolonged cycling and leaching of TM species, the nanoparticle has become near hollow. Nevertheless, its shell has remained a Pt-TM nanoalloy.

the composition, structure, stability and electrocatalytic activity of Pt-TM nanoalloys inside operating PEMFCs appears difficult to predict. To assess it, semi-empirical approximations found useful in connecting the composition and structure of bulk alloys with their preparation and electrocatalytic activity, such as Vegard's law, are often used.

D Deviations from Vegard's law related to the stability and electrocatalytic activity of Pt-TM Nanoalloys

Vegard's law predicts a steady linear change in the lattice parameter for continuous metallic alloys, including fcc-type Pt-TM alloys, wherein the distinct atomic species simply substitute for one another.[34] That is, the lattice parameter for fcc Pt_xTM_{100-x} alloys, a, would be

$$a(X) = a_{Pt}X + a_{TM}(1-X), \qquad (2)$$

where $0 < X < 100$ is the percentage of Pt in the nanoalloy, a_{Pt} and a_{TM} is the fcc-lattice parameter for pure Pt and TM metals, respectively. Note that *Eq.* 2 is considered applicable not only for binary but also ternary fcc-type Pt-TM alloys comprising Ni, Co and/or Cu because the atomic volume (see above) and lattice parameter (a_{Ni}=3.52 Å; a_{Co}(fcc)= 3.55 Å; a_{Cu}=3.62 Å) of these TM species are close to each other.[78]

Experimental fcc-lattice parameters for fresh and cycled Pt-TM alloy NPs (TM=Ni, Co and/or Cu) derived from *in operando* PDF data

are shown in Figure 7d. As can be seen in the Figure, the variation of the lattice parameter with the NP composition shows a large positive deviation from Vegard's law. This may not come as a big surprise because Vegard's law is indeed seldom perfectly obeyed.[79-81] In particular, in an ideal random fcc alloy at a given temperature, the constituent atoms are randomly distributed (ΔS is maximized) and the thermodynamic excess characteristics of the alloy, such as ΔH and eventual excess volume ΔV, are zero. The volume of the unit cell of the alloy is therefore a linear function of the volumes of the unit cells of the constituent pure metals. Since the fcc-lattice parameter is related to the fcc-cell volume by the relation $V_{(fcc\ cell)} = (a_{fcc})^3$, a linear dependence of $V_{(fcc\ cell)}$ on the relative percentage of the constituent atoms implies a non-linear variation of a_{fcc} on that percentage. Then, the dependence of the lattice parameter for an ideal Pt-TM random alloy on the percentage of Pt species, X, should indeed be expressed as

$$a(X) = \{V_{Pt}X + V_{TM}(1-X)\}^{1/3}, \qquad (3).$$

where V_{Pt} and V_{TM} are the rather different (by ~22 to 28 %) elemental volumes of atoms in pure Pt and TM metals, respectively. Accordingly, as shown in Figure 7d, the functional dependence of a(X) on X would show a positive deviation from Vegard's law, even for an ideal Pt-TM random alloy. When the alloy is not ideal, *e.g.* due to non-linear variation of the "size"/WS volume of the constituent atoms with its composition arising from valence charge redistribution, related atomic-level strain, chemical disordering effects, and others, the positive deviation from Vegard's law may appear even stronger, as exhibited by the experimental fcc-lattice parameters shown in Figure 7d. Generally, such a strong deviation from the law may be accounted for by introducing a quadratic correction term in *Eq.* 2 as follows [81,82]

$$a(X) = \{V_{Pt}X + V_{Tm}(1-X) + X(1-X)\Omega\}^{1/3}, \qquad (4)$$

where the quantity Ω may be interpreted as an "excess volume" arising from the "excess" differences in the WS volume (electron density distribution) of the constituent Pt and TM species in comparison to their volume in bulk Pt-TM alloys.[69,70,78] The "excess volume" would make an extra positive contribution to the "excess free energy" of Pt-TM nanoalloys, thus rendering them much less stable (*e.g.* melt at lower temperature) in comparison to their bulk counterparts.[74-77] Experimental data for the fcc-lattice parameter for fresh binary and ternary Pt-TM nanoalloy particles (TM=Ni, Co and/or Cu) with a largely different morphology (*e.g.* spheres, octahedra and wires), synthesized by different protocols, deposited on different supports (*e.g.* carbon and silica) and some annealed at very high temperature (*e.g.* 900 °C) for hours are summarized in Figure 7c. .[6,17-19,21-23,28,83] These data also exhibit a strong positive deviation from Vegard's law indicating that binary and ternary Pt-TM nanoalloys (TM=Ni, Co and/or Cu) are intrinsically much less stable than the corresponding ideal Pt-TM nanoalloys.[84] Therefore, evaluating the composition, degree of alloying and stability of Pt-TM nanoalloy particles from experimental data for their fcc-lattice parameter using the Vegard's law approximation, as defined by *Eq.* 2, and vice versa, may lead to contradicting results (*e.g.* see Figure 4 in Ref. [30] and Table 5 in Ref. [19]). On the other hand, when taken into consideration, observed deviations from Vegard's law can help evaluate the stability and, hence, activity of Pt-TM

nanoalloys as catalysts for the ORR taking place at the cathode of operating PEMFCs.

In particular, regardless strained (V_{TM} and V_{Pt} differing by more than 20 %; see Figure 7b), not quite random (ΔS not maximized; see model structures in Figure 6) and densely packed (Ω significantly > 0; see Figure 7d), fresh Pt-TM catalyst can remain intact under ambient conditions for a long time. Under the electrochemical conditions created by the high humidity, electrodes, at the temperature and gas flow in the operating PEMFC, the catalyst particles may need to adopt an energetically more favourable atomic-level structure. Considering the difference in the elemental "size", cohesive energy and reduction potential (-0.25 V for Ni, -0.28 V for Co and 0.5 V for Cu *vs.* 1.18 V for Pt) of the constituent Pt and TM atoms, one may expect that a dissolution of TM species from the particles would be favourable at least because it would reduce the compressive stresses on Pt species. In addition, it may be expected that a large fraction of TM species would leach from the particles pretty soon after the PEMFC starts operating. This is because the interdiffusion of atoms in nanoalloys is several orders of magnitude faster in comparison to bulk alloys.[85,86] The initial compressive strain and electrocatalytic activity of the nanoalloy particles would drop accordingly, regardless their GSA hardly changes. This is indeed what the experimental data in Figure 6 show. The resulting structural state, including the residual compressive strain, relative percentage and intermixing pattern of near surface Pt and TM species would largely determine the electrocatalytic activity of the so "activated" particles during the PEMFC operation. For any chemical composition of the fresh nanoalloy catalysts, the dissolution would carry on until the percentage of TM species, related atomic level strain and/or near surface relaxation effects leading to significant "excess volume" Ω in the functioning nanoalloy catalysts are reduced to a minimum, as observed here and elsewhere (follow the solid arrows in Figures 7c and 7d). For long periods of PEMFC operation, the dissolution may even render the nanoalloy particles hollow but not necessarily completely free of TM atoms, as shown in Figure 8d. That is because Pt and TM atoms remaining in the particles are free to search and adopt energetically more favourable configurations through fast interdiffusion, including partial re-alloying.[73,75,87,88] In the process, and strongly depending on their initial TM content and phase state, the nanoalloys may adopt transient structural states, *e.g.* fully TM core-thick Pt shell type structure (see data in Figure 6e), which have proven beneficial to the ORR kinetics.[6,89-92] Unless stabilized though, such states may degrade, thereby rendering the useful lifetime of nanoalloy catalysts shorter than desired. Regardless the sustained effort, this problem has not been fully solved yet.[26] Though seemingly not so severe,[30] the related problem with the excessive mass transport (see Figures 2, 3 and S6) eventually leading to activity losses due to Ostwald ripening, coalescing and/or and contamination of MEAs with dissolved TM species also has to be addressed*.*

Conclusions

Undoubtedly, *ex situ* characterization of nanoalloy electrocatalysts, including Pt-TM nanoalloys, is a necessary starting point of any effort to improve their stability and activity. However, it has to be recognized that fresh Pt-TM nanoalloys are merely pre-catalysts, and the actual catalysts are formed as deposited on MEAs and exposed to high humidity, elevated temperature and fast repetitive voltage pulses inside PEMFCs. Moreover, the chemical composition and nanophase state of the actual catalysts keep changing during their utilization leading to further changes in their activity. Naturally, for significantly different nanoalloys the changes differ significantly in dynamics and/or scope. Combined EDS and HE-XRD experiments make it possible to directly follow the evolution of Pt-TM nanoalloy catalysts from their initial state, to their active form and further along their usage with atomic-level precision (~ 0.02 Å) and element specificity (~ 2–3 at%), and link it to the resulting ORR activity losses in both time (~ 1 min) and space (~ μm) resolved manner. It is essential to study the dynamic behaviour of nanoalloy catalysts under operating conditions and derive meaningful relationships between relative changes in their composition, structure and electrocatalytic activity with respect to the initial state, and not to resort to imprecise approximation. The relationships will both help streamline the ongoing synthesis effort to produce better catalysts and inform the related to it theory. Together with other established techniques, *in operando* synchrotron x-ray spectroscopy and total scattering can assist this urgent scientific endeavour, thus bringing fuel cell technologies a step closer to commercialization.

Conflicts of interest

There are no conflicts to declare.

Acknowledgements

References

1. H. A. Gasteiger, S. S. Kocha, B. Sompalli and F. T. Wagner, *Appl. Catal B*, 2005, **56**, 9-35.
2. T. Toda, H. Igarashi and M. *J.* Watanabe, *Electrochem. Soc.*, 1998, **145**, 4185-4188.
3. L. Chen, H. Guo, T. Fujita, A. Hirata, W. Zhang, A. Inoue and M. Chen, *Adv. Funct. Mater.*, 2011, *21*, 4364-4370.
4. B. Hammer and J. K. Norskov, *Adv. Catal.*, 2000, **45**, 71-129.
5. L. Bu, N. Zhang, S. Guo, X. Zhang, J. Li, J. Yao, T. Wu, G. Lu, J. Y. Ma, D. Su and X. Huang, *Science*, 2016, **354**, 1410-1414.
6. P. Strasser, S. Koh, T. Anniyev, G. Greeley, K. More, C. Yu, Z. Liu, S. Kaya, D. Nordlund, H. Ogasawara, M. F. Toney and A. Nilsson, *Nat. Chem.*, 2010, **2**, 454-460.
7. X. Huang, L. Zhao, L. Cao, Y. Chen, E. Zhu, Z. Lin, M. Li, A. Yan, A. Zettl, Y.M. Wang, X. Duan, T. Mueller, and Y. Huang, *Science*, 2015, **348**, 1230-1234.
8. V. R. Stamenkovic, B. S. Mun, K. J. J. Mayrhofer, P. N. Ross and N. M. Markovic, *J. Am. Chem. Soc.* 2006, **128**, 8813-8819.
9. M. Mavrikakis, B. Hammer and J. K. Norskov, *Phys. Rev. Lett.* 1998, **81**, 2819-2822.
10. F. Maroun, F. Ozanam, O.M. Magnussen and R. J. Behm, *Science* 2001, **293**, 1811-1814.

11. V. R. Stamenkovic, B. S. Mun, M. Arenz, K. J. J. Mayrhofer, C. A. Lucas, G. Wang, P. N. Ross and N. M. Markovic, *Nat. Mater*. 2007, **6**, 241-247.

12. S. Mukerjee, S. Srinivasan, M. P. Soriaga and J. McBreen, *J. Electrochem. Soc*. 1995, **142**, 1409-1422.

13. B. N. Wanjala, R. Loukrampam, J. Luo, P. N. Njoki, D. Mott, C. J. Zhong, M. Shao, L. Protsailo and T. Kawamura, *J. Phys. Chem*. 2010, **14**, 17580-17590.

14. C. Cui, L. Gan, M. Heggen, S. Rudi and P. Strasser, *Nat. Mater.* 2013, **12**, 765-771.

15. C. Chen¸ Y. Kang, Z. Huo, Z. Zhu, W. Huang, H. L. Xin, J. D. Snyder, D. Li, J. A. Herron, M. Mavrikakis, M. Chi, K. L. More, Y. Li, N. M. Markovic, G. A. Somorjai, P. Yang and V. R. Stamenkovic, *Science* 2014, **343**, 1339-1343.

16. W. D. Callister, *John Wiley & Sons*, New York, 2007.

17. C. Cui, L. Gan, M. Neumann, M. Heggen, B. R. Cuenya and P. Strasser, *J. Am. Chem. Soc.* 2014, **136**, 4813-4816.

18. G. Greco, A. Witkowska, M. Minicucci, L. Olivi, E. Principi, S. Dsoke, A. Moretti, R. Marassi and A. Di Cicco, *J. Phys. Chem. C* 2012, **116**, 12791-12802.

19. D. Wang, P. Zhao, Y. Li, *Sci. Rep.* 2011, **1**, 37.

20. K. Jiang, D. Zhao, S. Gou, X. Zhang, X. Zhu, J. Guo, G. Lu and X. Huang, *Sci. Adv.* 2017, **3**, e1601705.

21. S. Mezzavilla, C. Baldizzone, A. C. Swertz, N. Hodnik, E. Pizzutilo, G. Polymeros, G. P. Keeley, J. Knossalla, M. Heggen, K. J. J. Mayrhofer and F. Schüth, *ACS Catal*. 2016, **6**, 8058-8068.

22. L. Gan, M. Hegen, S. Rudi and P. Strasser, *Nano Lett*. 2012, **12**, 5423-5430.

23. M. Oezaslan and P. Strasser, *J. Power Sources* 2011, **196**, 5240-5249.

24. S. L. Choi, S. Xie, M. Shao, J. H. Odell, N. Lu, H. C. Peng, L. Protsailo, S. Guererro, J. Park, X. Xia, J. Wang, M. J. Kim and Y. Xia, *Nano Lett*. 2013, **13**, 3420-3425.

25. P. Strasser and S. Kühl, *Nano Energy* 2016, **29**, 166-177.

26. S. Cherevko, N. Kulyk and K. J. J. Mayrhover, *Nano Energy* 2016, **29**, 275-298.

27. Y. J. Wang, N. Zhao, B. Fang, H. li, X.T. Bi and H. Wang, *Chem. Rev*. 2015, **115**, 3433-3467.

28. G. C. K. Liu, D. A. Stevens, J. C. Burns, R. J. Sanderson, G. Vernstrom, R. T. Atanasoski, M. K. Debe and J. R. Dahn, *J. Electrochem. Soc*. 2011, **158**, B919-B926.

29. J. A. Gilbert, A. J. Kropf, N. N. Kariuki, S. DeCrane, X. Wang, S. Rasouli, K. Yu, P. J. Fereira, D. Morgan and D. J. Meyers, *J. Eletrochem. Soc*. 2015, **162**, F1487-F1497.

30. D. D. Papadias, R. K. Ahluwalia, N. Kariuki, D. Myers, K. L. More, D. A. Cullen, B. T. Sneed, K. C. Neyerlin, R. Mukundan and R. L. Borup, *J. Electrochem. Soc*. 2018, **165**, F3166-F3177.

31. Q. Jia, W. Liang, M. K. Bates, P. Mani, W. Lee and S. Mukerjee, *ACS Nano* 2015, **9**, 387-400.

32. M. Watanabe, D. A. Tryk, M. Wakisaka, H. Yano and H. Uchida, *Electrochimica Acta* 2012, **84**, 187-201.

33. D. E. Ramaker, A. Korovina, V. Croze, J. Melke and C. Roth, *Phys. Chem. Chem. Phys.* 2014, **16**, 13645-13653.

34. L. Z. Vegard, *Kristallogr*. 1928, **67**, 239-259.

35. V. Petkov, Y. Maswadeh, Y. Zhao, A. Lu, H. Cronk, F. Chang, S. Shan, H. Kareem, J. Luo, C. J. Zhong, C. J. Shastri and P. Kenesei, *Nano Energy* 2018, **49**, 209-220.

36. R. Borup, J. Meyers, B. Pivovar, Y. S. Kim, R. Mukundan, N. Garland, D. Myers, M. Wilson, F. Garzon, D. Wood, P. Zelenay, K. More, K. Stroh, T. Zawodzinski, J. Boncella, J. E. McGrath, M. Inaba, K. Miyatake, M. Hori, K. Ota, Z. Ogumi, S. Miyata, A. Nishikata, Z. Siroma, Y. Uchimoto, K. Yasuda, K. I. Kimijima and N. Iwashita, *Chem. Rev.* 2007, **107**, 3904-3951.

37. S. Takahisa and Y. Morimoto, *Electrochemistry* 2016, **84**, 511-515.

38. V. Saveleva,V. Papaefthimiou,M. K. Daletou, V. H. Doh, C. Ulhaq-Bouillet, M. Diebold, S. Zafeiratos and L. R. Savinova, *J. Phys. Chem. C* 2016, **120**, 15930–15940.

39. C. A. Rice, P. Urchaga, A. O. Pistono, B. W. McFerrin, B. T. McComb and J. Hu, *J. Electrochem. Soc.* 2015, **162**, F1175-F1180.

40. M. Uchimura and S. Kocha, *ECS Transactions,* 2007, **11**, 1215-1226.

41. E. Antolini, J. R. C. Salgado and E. R. Gonzalez, *J. Power Sources* 2006, **160**, 957-968.

42. Y. Huang, J. Zhang, A. Kongkanand, F. T. Wagner, J. C. M. Li and J. Jorne, *J. Electrochem. Soc*. 2014, **161**, F10-F15.

43. R. Jinnouchi, K. Kodama, Y. Hatanaka and Y. Morimoto, *Phys. Chem. Chem. Phys*., 2011, **13**, 21070–21083.

44. J. K. Norskov, J. Rossmeisl, A. Logadottir, L. Lidqvist, J. R. Kitchin, T. Bligaard and H. Jonsason, *J. Phys. Chem. B* 2004, **108**, 17886-17892.

45. H. Schmies, A. Bergmann, J. Drnec, G. Wang, D. Teschner, S. Kühl, D. J. S. Sandbeck, S. Cherevko, M. Gocyla, M. Shviro, M. Heggen, V. Ramani, R. E. Dunin-Borkowski, K. J. J. Mayrhofer and P. Strasser, Adv. Ener. Mater. 2017, **4**, 1701663.

46. I. E. L. Stephens, J. Rossmeisl, I. Chorkendorff, *Science* 2016, **354**, 1378-1379.

47. S. Martens, L. Asen, G. Ercolano, Ch. Zalitis, A. Hawkins, A. M. Bonastre, L. Seidl, A. C. Knoll, J. Sharman, P. Strasser, D. Jones and O. Schneider *J. Power Sources* 2018, *392*, 274-284.

48. S. D. Shastri, J. Almer, C. Ribbing and B. Cederstřom, *J. Synchrotron Radiat.* 2007, **14**, 204–211.

49. P. K. Klug and L. E. Alexander, *Wiley*, 1974.

50. E. F. Holby, W. Sheng, Y. Shao-Horn and D. Morgan, *Energy Environ. Sci.,* 2015, **8**, 258-266

51. V. Petkov, B. Prasai, S. Shastri, H. U. Park, Y. U. Kwon and V. Skumryev, *Nanoscale* 2017, **9**, 15505-15514.

52. D. E. Newbury, *Wiley*, 2002.

53. H. Baker, *ASM INTERNATIONAL*, 1992.

54. C. L. Farrow, P. Juhas, J. W. Liu, D. Bryndin, E. S. Bozin, J. Bloch, T. Proffen and S. J. L. Billinge, *J. Phys.: Condens. Matter*. 2007, **19**, 335219.

55. W. H. Qi and M. P. Wang, *J. Nanopart. Res.* 2005, **7**, 51-57.

56. S. I. Sanchez, M. W. Small, E. S. Bozin, J. G. Wen, J. M. Zuo and R. G. Nuzzo, *ACS Nano* 2013, **7**, 1542-1557.

57. J. X. Wang, C. Ma, Y. Choi, D. Su, Y. Zhu, P. Liu, R. Si, M. B. Vukmirovic, Y. Zhang and R. Adzic, *J. Am. Chem. Soc*. 2011, **133**, 13551-13557.

58. A. Navrotsky, *ChemPhysChem*, 2011, **12**, 2207-2215.

59. B. Prasai, A. R. Wilson, B. J. *Wiley*, Y. Ren and V. Petkov, *Nanoscale*, 2015, **7**, 17902-17922.

60. S. Plimpton, *J. Comp. Phys.* 995, **117**, 1-19. http://lammps.sandia.gov.

61. J. S. Kim, D. Seol, J. Ji, H. S. Jang, Y. Kim and B. J. Lee, *Calphad*, 2017, **59**, 131-141.

62. P. K. Klug, L. E. Alexander, *Wiley*, 1974.

63. Y. Maswadeh, Sh. Shan, B. Prasai, Y. Zhao, Zh. Xie, Zh. Wu, J. Luo, Y. Ren, C. J. Zhong and V. Petkov, *J. Mat. Chem. A* 2017, **5**, 7355-7365.

64. R. M. Arán-Ais, F. Dionigi, T. Merzdorf, M. Gocyla, M. Heggen, R. E. Dunin-Borkowski, M. Gleich, J. Solla-Gullón, E. Herrero, J. M. Feliu and P. Strasser, *Nano Lett.* 2015, **15**, 7473-7480.

65. R. Loukrakpam, S. Shan, V. Petkov, L. Yang, J. Luo and C. J. Zhong *J. Phys. Chem.* C 2013, **117**, 20715-20721.

66. S. Shan, J. Luo, J. Wu, N. Kang, W. Zhao, H. Cronk, Y. Zhao, P. Joseph, V. Petkov, V. and C. J. Zhong, *RCS Adv*. 2014, **4**, 42654-42669.

67. B. N. Wangala, B. Fang, R. Loukrakpam, Y. Chen, M. Engelhard, J. luo, J. Yin, L. Yang, S. Shan and C. J. Zhong, *ACS Catal*. 2012, **2**, 795-806.

68. M. Sigalas, M., Papaconstantopoulos, D. A. and N. C. Bacalis, *Phys. Rev. B* 1992, **45**, 5777-5783.

69. L. Pauling, *Proc. Natl. Acad. Sci. U. S. A*. 1950, **36**, 533–538.

70. L. Pauling, *Cornell University Press*: Ithaca, NY, 1975.

71. T. Rajasekharan and V. Seshubai, *Acta Crystallogr., Sect. A: Found. Crystallogr.* 2012, **68**, 156–165.

72. Note that, as discussed in ref. [45], losses in hydrogen adsorption/desorption-determined ECSA do not necessarily reflect well all losses in the number (density) of surface Pt atoms capable of reducing O_2 . Hence, we differentiate between the sudden drop in the apparent ORR activity, caused by initial fast structural changes, such as nanophase transitions and strain relaxation, and further gradual losses in apparent ORR activity, caused by a gradual decrease in the GSA/ECSA due to NP growth and coalescing. That is because GSA/ECSA of Pt-TM NPs hardly changes within the first 30-50 min of the PEMFC operation (see data in Figure 6).

73. A. R. Miedama, P. F. de Chatel and F. R. de Boer, *Physica B+C* 1980, **100**, 1-28.

74. R. Ferrando, J. Jellinek and R. L. Johnston, *Chem. Rev*. 2008, **108**, 845–910.

75. L. L. Wang and D. D. Johnson, *J. Am. Chem. Soc.* 2009, **131**, 14023-14029.

76. P. K. Ray, M. Akinc and M. J. Kramer, *J. Alloys and Compd*., 2010, **489**, 357-361.

77. L. Vitos, A. V. Ruban, H. L. Skriver and J. Kollár, *Surf. Sci.* 1998, **411**, 186–202.

78. R. W. G. Wykoff, Beinhold Publishing Co.: NY, 1955.

79. K. A. Gschneider Jr. and G. H. D. Vineyard, *Appl. Phys*. 1962, **33**, 3444-3450.

80. A. R. Denton and N. W. Ashcroft, *Phys. Rev. A* 1991, **43**, 3161-3164.

81. V. A. Lubarda, *Mechan. Mater*. 2003, **35**, 53-68.

82. K. T. Jacob, S. Raj and L. Rannesh, *J. Mater. Res*. 2007, **49**, 776-779.

83. S. M. Alia, C. Ngo, S. Shulda, M. A. Ha, A. A. Dameron, J. N. Weker, K. C. Neyerlin, S. Kocha, S. Pylypenko and B. S. Pivovar, *ACS Omega* 2017, **2**, 1408–1418.

84. Note that the non-linearity can be discerned directly from experimental XRD patterns for the nanoalloys (*e.g.* Figure S14).

Because of their diffuse character though, the patterns are less sensitive to the atomic-level structure of nanoalloys in comparison to their Fourier counterparts, the respective atomic PDFs. That is because atomic PDFs take into account both the Bragg-like and diffuse component of the diffraction data and, furthermore, do not imply any periodicity.

85. Q. Zhang, J. Y. Lee, J. Yang, C. Boothroyd, J. Zhang, *Nanotechnology* 2007, **18**, 245605.

86. H. Yasuda and H. Mori, *Phys. Rev. Lett*. 1992, **69**, 3747–3750.

87. V. Petkov, Y. Maswadeh, Y. Zhao, A. Lu, H. Cronk, F. Chang, S. Shan, H. Kareem, J. Luo, C. J. Zhong, S. Shastri and P. Kenesei, *Nano Energy* 2018, **49**, 209-220.

88. V. Petkov, B. Prasai, S. Shan, Y. Ren, J. Wu, H. Cronk, J. Luo and C. J. Zhong, *Nanoscale* 2016, **8**, 10749-10767.

89. P. Malacrida, M. Escudero-Escribano, A. Verdaguer-Casadevall, I. E. L. Stephens and I. Chorkendorff, *J. Mater. Chem. A* 2014, **2**, 4234-4243.

90. S. Kaneko, R. Myochi, Sh. Takahashi, N. Todoroki, T. Wadayama and T. Tanabe, *J. Phys. Chem. Lett.* 2017, **8**, 5360–5365.

91. M. Escudero-Escribano, P. Malacrida, M. H. Hansen, U. G. Vej-Hansen, A. Velázquez-Palenzuela, V. Tripkovic, J. Schiøtz, J. Rossmeisl I. E. L Stephens and I. Chorkendorff, *Science*, 2016, **352**, 73-76.

92. F. Chang, G. Yu, S. Shan, Z. Skeete, J. Wu, J. Luo, Y. Ren, V. Petkov and C. J. Zhong, *J. Mater. Chem. A,* 2017, **5**, 12557–12568.

TOC